Bach, C., Hainzl, S. (2012): Improving empirical aftershock modeling based on additional source information. - Journal of Geophysical Research, 117, B04312

DOI: 10.1029/2011JB008901

Improving empirical aftershock modeling based on additional source information

C. Bach[1] and S. Hainzl[1]

Received 23 September 2011; revised 28 February 2012; accepted 29 February 2012; published 24 April 2012.

[1] Several mechanisms are proposed to underlie earthquake triggering including static stress interactions and dynamic stress transfer. Significant differences of these mechanisms are particularly expected in the spatial distribution of aftershocks. However, testing the different hypotheses is challenging because it requires the consideration of the large uncertainties involved in stress calculations as well as the appropriate consideration of secondary aftershock triggering which is related to stress changes induced by smaller pre- and aftershocks. In order to evaluate the forecast capability of different mechanisms, we take the effect of smaller-magnitude earthquakes into account by using the epidemic type aftershock sequence (ETAS) model where the spatial probability distribution of direct aftershocks, if available, is correlated to alternative source information and mechanisms. We test surface shaking, rupture geometry, and slip distributions. As an approximation of the shaking level, we use ShakeMap data which are available in near real-time after a main shock and thus could be used for first-order forecasts of the spatial aftershock distribution. Alternatively, we test the use of empirical decay laws related to minimum fault distance and Coulomb stress change calculations based on published and random slip models. For comparison, we analyze the likelihood values of the different model combinations in the case of several well-known aftershock sequences (1992 Landers, 1999 Hector Mine, 2004 Parkfield). Our test shows that the fault geometry is the most valuable information for improving aftershock forecasts. Furthermore, we find that static stress maps can additionally improve the forecasts of off-fault aftershock locations, while the integration of ground shaking data could not upgrade the results significantly.

Citation: Bach, C., and S. Hainzl (2012), Improving empirical aftershock modeling based on additional source information, *J. Geophys. Res.*, *117*, B04312, doi:10.1029/2011JB008901.

1. Introduction

[2] Aftershock activity following large earthquakes is well known. Although it seems to be clear that the main shock induced stress and state changes are the origin of aftershock activity, the main triggering mechanism is still controversially discussed. The proposed mechanisms of static and dynamic stress changes [*Harris*, 1998], afterslip [*Perfettini and Avouac*, 2007] and poro-elastic effects [*Nur and Booker*, 1972; *Cocco and Rice*, 2002] differ in particular in their prediction of the spatial aftershock distribution. However, a comparative evaluation and application of these models is challenging because they all need additional information and parameter settings. Thus it is still not clear whether those physics-based aftershock models can improve statistical models for practical forecasting.

[3] Recently, *Woessner et al.* [2011] showed for a retrospective short-term (90 days) forecast of the 1992 Landers aftershock sequence that purely statistical models, in particular the ETAS model, seem to outperform physics-based models with regard to their forecasting ability. The basic assumption of the epidemic type aftershock sequence (ETAS) model [*Ogata*, 1988, 1998] is that every event is increasing the probability of new events according to empirical relations for the magnitude-dependent productivity and the spatial and temporal aftershock distributions. The temporal aftershock decay is described by the Omori-Utsu law, which has been successfully applied to many aftershock sequences [*Utsu et al.*, 1995]. This law states that the number of nucleating aftershocks decays proportional to $(t + c)^{-p}$ with elapsing time t from the main shock, where c and p are constants. Based on the formulation of *Utsu and Seki* [1955], from the relations between magnitude and rupture area as well as between the rupture area and the number of aftershocks is concluded that the aftershock productivity is proportional to $\sim e^{\alpha M}$ in agreement with observations [*Helmstetter et al.*, 2005; *Marsan and Lengliné*, 2008]. Here, the parameter α is a measure of the magnitude-dependent triggering capability. And finally, the aftershock distribution in space is assumed to follow a power law decay as a function of the distance to the source which is in good agreement with recent observations [*Marsan and Lengliné*, 2010].

[1]GFZ German Research Centre for Geosciences, Potsdam, Germany.

0148-0227/12/2011JB008901

Table 1. Different Tested Model Combinations and Their Necessary Input Information for Modeling the Spatial Aftershock Distribution[a]

Model	Used Main Shock Information			
	Epicenter	ShakeMap	Fault Geometry	Slip Model
$ETAS_{basic}$	X			
$ETAS_{ShakeMap}$		X		
$ETAS_{GMM}$			X	
$ETAS_{basic+fault}$			X	
$ETAS_{\Delta CFS(random\ slip)}$			X	
$ETAS_{\Delta CFS}$			X	X
$ETAS_{\Delta CFS+ShakeMap}$		X	X	X

[a]For a detailed description of the individual models see section 2.

[4] While the empirical laws for the magnitude-dependence and the temporal decay can be simply applied based on earthquake catalog information, the application of the spatial distribution law leads to forecasts of isotropic aftershock clouds which are clearly in contradiction to the observed anisotropic aftershock patterns. In nature, aftershock populations are mainly triggered along the whole rupture length and not only clustered around the main shock epicenters. Thus, to improve aftershock forecasts, additional consideration concerning the spatial occurrence probabilities is obviously needed. In this paper, we test the value of additional information regarding the rupture geometry, measured and modeled spatial distribution of ground shaking and calculations of static stress changes.

[5] The aim is to develop hybrid models using additional information according to their availability (see Table 1). In general, the first available information is the main shock magnitude and position, beside information about preceding seismic activity. In this case, using the ETAS model provides a rough estimate of the aftershock distribution. However, based only on hypocenter locations, the ETAS model predicts an isotropic spatial clustering, this clearly contradicts the usually elongated shape of fault zones and aftershock activity.

[6] Therefore, it is necessary to use quickly available spatial enhancements. ShakeMaps are available in near real time and provide interpolated maps of observed surface ground motions following significant earthquakes. Peak ground velocity is a proxy for dynamic stress, which is typically highest near the ruptured fault and is proposed to be the triggering mechanism for aftershocks [*van der Elst and Brodsky*, 2010]. Therefore using ShakeMaps, based on measured and interpolated ground shaking, seems to be a good opportunity to improve the spatial aftershock estimation. However, ShakeMap data might be contaminated by near surface effects. Thus, if the rough geometry of the ruptured fault is known, we can alternatively use ground motion estimations based on ground motion models for hard rock (GMMs). Another possibility in the case of known fault geometry is to use seismicity based decay functions which are derived by fitting the ETAS model to precursory seismicity. That means, we can test the application of the empirical spatial ETAS kernel which is now evaluated as a function of the nearest distance to the rupture area and not to the epicenter location. If in addition also a slip model is available, the information of calculated Coulomb stress change (ΔCFS) maps can be helpful because ΔCFS values have been found to be often correlated to the aftershock distributions [*King et al.*, 1994; *Harris*, 1998]. In absence of slip inversions, we can use random slip distribution for the Coulomb stress calculations based solely on the fault geometry and the main shock magnitude. *Steacy* [2004] already showed that the correct rupture geometry is the most important input for static stress change calculations. When using greatly simplified slip, calculated stress fields would only differ very close to the fault plane from that based on a time-consuming slip inversion.

[7] In this paper we systematically test the value of those additional source information for improving the spatial aftershock forecasts. The test is applied to three well-known aftershock sequences in California, namely the 1992 Landers, the 1999 Hector Mine and the 2004 Parkfield earthquake sequences. We first introduce the model approach in section 2 and present the data for the test cases in section 3. In sections 4 and 5, we then discuss the results for the three test cases and investigate the influence of cut-off magnitude, time window and parameters changes. Our conclusions are discussed and summarized in sections 6 and 7.

2. Model

[8] Our model approach is focused on the improvement of the spatial forecasts of those aftershocks directly triggered by the main shocks. For this purpose we make use of additional source information which are typically available for main shocks. To do this in the most robust way, we implement the additional information within the framework of the epidemic type aftershock sequence (ETAS) model, which has become the standard model for earthquake clustering in the recent years. It is a stochastic point-process model based on the well-known empirical characteristics of timing and magnitude-dependence mentioned above and takes into account stationary seismicity as well as secondary aftershock triggering [*Ogata*, 1988; *Helmstetter and Sornette*, 2002]. In the ETAS model, each event is seen as a potential main shock, however, with an aftershock trigger potential which scales exponentially with the earthquake magnitude, namely $Ke^{\alpha(M-M_{\min})}$. Here α and K are model parameters and $M_{\min}$ is the lower magnitude cut-off of the earthquakes under consideration. The total occurrence rate of earthquakes is given by

$$\lambda(t,\vec{x}) = \mu + \sum_{i:t_i<t} \frac{Ke^{\alpha(M_i-M_{\min})}}{(t-t_i+c)^p} f_i(\vec{x}), \qquad (1)$$

where μ is a constant background rate, modeled by a stationary Poisson process, and c and p are the parameters of the Omori-Utsu law. For simplicity, we assume a uniform background rate because the estimation of space dependence would require rather arbitrary smoothing procedures of precursory background seismicity. However, the difference compared to the use of space dependent background rates is expected to be small because the background rate is additive in the ETAS formulation and the considered time periods are small. In the general case of having only earthquake catalog information (time, epicenter and magnitude),

the spatial function is necessarily isotropic and is often modeled by a power law decay [*Console et al.*, 2003, 2006; *Hainzl et al.*, 2008],

$$f_i(\vec{x}) = f_{iso}(\vec{x} - \vec{x}_i) = \frac{(q-1)d^{2(q-1)}}{\pi[|\vec{x} - \vec{x}_i|^2 + d^2]^q}, \quad (2)$$

where d and q are two free parameters. In the following, this model is called $\mathrm{ETAS}_{\mathrm{basic}}$.

[9] Now we assume that we have external information about the spatial probability distribution of the direct aftershocks, $f_m(\vec{x})$, for the main shock(s) with index m. The specific functions $f_m(\vec{x})$ depend on the chosen model which are presented in the following subsections. Then the direct extension of the basic ETAS model leads to

$$\lambda(t,\vec{x}) = \mu + \sum_{m:t_m<t} \frac{Ke^{\alpha(M_m - M_{\min})}}{(t - t_m + c)^p} f_m(\vec{x}) + \sum_{k:t_k<t} \frac{Ke^{\alpha(M_k - M_{\min})}}{(t - t_k + c)^p} f_{iso}(\vec{x} - \vec{x}_k), \quad (3)$$

where k denotes the index of the smaller magnitude events for which we have no additional source information.

[10] In the following subsections, it is shown how we calculated the spatial probability distributions $f_m(\vec{x})$ for the direct aftershocks in the case of different levels of input information and different assumptions about the underlying triggering mechanism. For a summary of all tested models with their necessary input information, see Table 1.

2.1. ShakeMap Information: $\mathrm{ETAS}_{\mathrm{ShakeMap}}$

[11] Beside earthquake catalog data, ShakeMaps are usually the quickest available information. ShakeMaps characterize the extent and distribution of strong ground shaking following significant earthquakes worldwide. Shaking is a dynamic effect limited in time and decreasing for larger distance. The effect of shaking is expected to be always positive, that means, aftershocks are stimulated which is consistent with the ETAS formulation. The maps are constrained partly by ground motions and by intensity data coupled with rupture dimensions resolved with rapid finite-fault analyses [*Wald et al.*, 2008]. Observations of peak ground acceleration (PGA) and velocity (PGV) are interpolated by ground motion models in areas of sparse station coverage.

[12] Because the peak dynamic strain can be assumed to be proportional to the PGV, the intensity of triggered aftershocks is expected to be simply proportional to the PGV in the case of dynamic stress triggering [*van der Elst and Brodsky*, 2010]. Thus, we assume in this case $f_m(\vec{x}) = C^{-1} \cdot PGV(\vec{x})$ with C being the normalization constant determined by $C = \int PGV(\vec{x})d\vec{x}$.

2.2. Ground Motion Model: $\mathrm{ETAS}_{\mathrm{GMM}}$

[13] As an alternative to ShakeMaps, we also use ground motion models (GMM) to estimate the PGV related to the main shock. In contrast to the ShakeMaps, these maps do not contain any direct ground shaking measurements, but on the other hand they cannot be contaminated by near surface effects, so-called site effects. The calculations require the knowledge of the rupture geometry to estimate the distance dependent PGV. For our PGV estimations, we make use of the ground motion relation developed within the NGA-project by *Campbell and Bozorgnia* [2008]. The probability map for aftershocks is then obtained by normalizing the PGV values. Please note that also this model is in general agreement with the ETAS approach because shaking is only assumed to activate, not to deactivate.

2.3. Empirical Fault Distance Relation: $\mathrm{ETAS}_{\mathrm{basic+fault}}$

[14] Beside GMM, we use an empirical aftershock decay law for modeling the anisotropic spatial aftershock distribution. In this case, we adopt the spatial ETAS kernel (equation (2)) which involves two free parameters and the distance to the source. In agreement with the GMM case, the decay law is now calculated using the minimum distance to the ruptured fault. This is in contrast to the basic ETAS model where the distance is always calculated relative to the epicenter. The two parameters of the decay function, d and q, are assumed to be the same for the anisotropic and the isotropic case and set by fitting pre-main shock events. Note that the spatial distribution has to be explicitly normalized for the anisotropic case, while the function is already normalized in the isotropic case.

2.4. Static Coulomb Failure Stress Change Maps: $\mathrm{ETAS}_{\Delta\mathrm{CFS}}$

[15] Aftershock distributions and the spatial patterns of static Coulomb Failure Stress changes (ΔCFS) are often found to be correlated, with more aftershocks in areas of positive than in areas of negative stress changes [*Harris*, 1998]. In particular, at distances greater than a few kilometers from the fault, the best correlations of Coulomb stress change with aftershock distributions have been observed [*King et al.*, 1994]. On a fault of a given orientation, the Coulomb stress change is defined according to

$$\Delta CFS = \Delta\tau + \mu(\Delta\sigma_n + \Delta P), \quad (4)$$

where $\Delta\tau$ is the shear stress change in slip direction, $\Delta\sigma_n$ the normal stress change, ΔP the pore pressure change and μ the coefficient of friction [*Harris*, 1998].

[16] Static stress triggering has been questioned because correlations between calculated stress and aftershock activity are typically not very high [*Hardebeck et al.*, 1998] and aftershocks occur also in stress shadows where the model predicts a decrease in seismicity rate [*Marsan*, 2003]. Recently, it has been shown that this apparent contradiction can be resolved by taking the involved small-scale slip variability and the large uncertainties of stress calculations into account [*Marsan*, 2006; *Hainzl et al.*, 2009]. In general, the calculation of Coulomb stress changes involves large uncertainties because of (1) the non uniqueness of slip inversions, (2) the unknown receiver fault mechanisms, (3) undetectable small-scale variations of slip and fault geometry, which can lead to strong stress heterogeneities close to the source fault, and (4) spatial inhomogeneity of material and prestress conditions [*Hainzl et al.*, 2009].

[17] ΔCFS calculations require the slip distribution of the earthquake and the definition of the geometry of the receiver faults on which stress perturbations are calculated. We use

Table 2. Information Related to the Slip Models and Standard Deviations Used for Coulomb Stress Calculations[a]

	1992 Landers	1999 Hector Mine	2004 Parkfield
Magnitude	7.3	7.1	6.0
Slip model	*Wald and Heaton* [1994]	*Ji* [2002]	*Custódio et al.* [2005]
Depth layers	3–13 km	3–13 km	3–13 km
Receiver fault strike	330° ± 20°	335° ± 20°	140° ± 20°
Receiver fault dip	90° ± 20°	80° ± 20°	87° ± 20°
Receiver fault rake	−180° ± 20°	−180° ± 20°	−180° ± 20°

[a]Strike and dip values are chosen according to the average main shock mechanism, rake value according to the general tectonic regime in California.

published slip models for our tests (Table 2). However, because reliable slip inversions are usually not available very quickly, we additionally test the use of random slip models. In this case, the spatial probability distribution results from averaging the probability maps of many random slip realizations, where each slip model is constrained by the fault geometry and the earthquake magnitude. The random slip is tapered toward the margin and high frequencies are damped using a k^{-2} slope, k is the radial wave number [*Herrero and Bernard*, 1994].

[18] For the receiver fault geometry, two concepts are commonly used. In both cases Coulomb stress changes are only calculated on one particular fault orientation, either on a manually predefined fixed plane or on the optimally oriented fault plane where the Coulomb stress is locally maximum. Both cases are not very realistic because choosing the relevant fault plane involves uncertainties and the seismogenic crust is typically fractured in a complex way. Thus, receiver faults in nature will have a number of orientations where earthquakes are able to nucleate.

[19] We take these uncertainties into account by using variations of receiver fault orientations, and by calculating the Coulomb stress change at several depth layers. In the following applications, we assume that the average mechanism of the aftershocks is identical to that of the main shock. Then we calculate the stress changes for a large number of receiver mechanisms which are taken randomly from Gaussian distributions for the strike, dip and rake values according to *Hainzl et al.* [2010a]. Here, we assume that the distributions of the aftershock mechanisms are homogeneous in space.

[20] To translate the calculated stress changes into an aftershock probability map, we utilize the clock advance model introduced by *Hainzl et al.* [2010b]. Based on basic assumptions, this model yields the general prediction that the number of aftershocks is directly proportional to ΔCFS in the case of positive stress changes while no aftershocks are expected in regions with negative stress changes. For N randomly selected aftershock mechanisms and Z depth layers, the aftershock probability map according to this model is given by

$$f_m(\vec{x}) = C^{-1} \sum_{k=1}^{Z} \sum_{i=1}^{N} \Delta CFS_{ik}(\vec{x}) H(\Delta CFS_{ik}(\vec{x})), \qquad (5)$$

where H denotes the Heaviside function ($H(s) = 1$ for $s \geq 0$ and 0 else). Here, the constant C is again given by normalization, that means by the constraint that $\int f_m(\vec{x}) d\vec{x} = 1$.

[21] The static stress triggering model is in general not consistent with the ETAS model due to the prediction of areas with suppressed activity (relative to the background rates) while the ETAS model only accounts for activation. This is less problematic because the number of missing events related to negative stress change will be very small on the short timescales considered here. Furthermore, by consideration of the uncertainties in the stress calculation, regions of expected seismic quiescence will vanish [*Hainzl et al.*, 2010a]. It is the same in our case, where almost in all locations the calculated aftershock rate is significantly larger than the background rate. Thus also the addition of the constant background rate in the ETAS model (which is not completely consistent with the stress-trigger model) will not affect the results significantly.

2.5. Combination of Static and Dynamic Stress Change: $ETAS_{\Delta CFS+ShakeMap}$

[22] In reality, static and dynamic stress triggering might act simultaneously. According to the analysis of *van der Elst and Brodsky* [2010], dynamic stress changes are responsible for approximately 50% of the aftershock generation. Thus we test one model in which both ShakeMap and ΔCFS probability maps are combined with equal weights.

3. Data

[23] Three different Californian earthquakes and their aftershock sequences are used to test the models. In particular, we apply the test for the 1992 M7.3 Landers, the 1999 M7.1 Hector Mine, and the 2004 M6.0 Parkfield earthquake. We have chosen a temporal window of 300 days before the main shock for optimizing the ETAS parameters and 300 days of aftershocks as the testing period for all models, the spatial window is chosen according to the coverage of the ShakeMap. In the case of Landers and Hector Mine, we use the relocated catalog by *Shearer et al.* [2005] to get precise epicenter information. The Landers sequence contains 1765 $M \geq 3$ events, 1474 are aftershocks, 291 events occur during 300 days before the main shock. The Hector Mine sequence contains 813 events matching the magnitude, time and space conditions, where 699 events are aftershocks and 114 occurred before the main shock. For the Parkfield sequence, the ANSS catalog is used (http://www.ncedc.org/cnss/) consisting of 436 $M \geq 3$ events with 93 foreshocks and 343 aftershocks. The ShakeMap data are freely available at the USGS webpage (http://earthquake.usgs.gov/earthquakes/shakemap/).

[24] For the calculation of the Coulomb stress changes, we utilize the software of *Wang et al.* [2006] for a layered half-space. In each case, the same 1D-velocity model is used as for the slip inversions. The slip models are taken from the finite-source rupture model database maintained by Martin

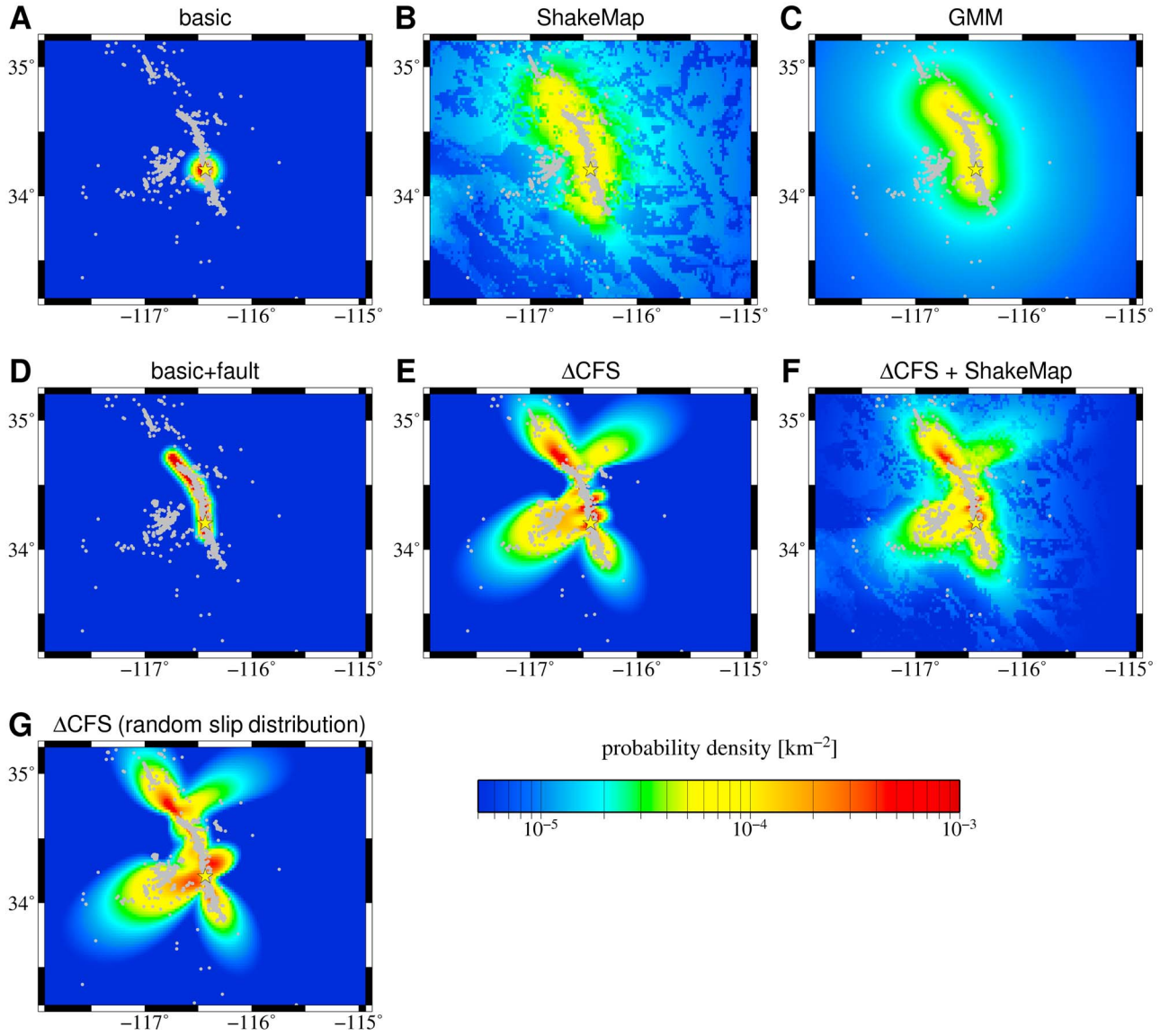

Figure 1. Calculated probability maps for the Landers earthquake. (a) Probability map used in the basic ETAS model. (b–g) Probability maps based on ShakeMap, GMM, the ETAS spatial kernel applied to the nearest distance to the ruptured fault, ΔCFS, a combination of ΔCFS and ShakeMap data and ΔCFS based on random slip distributions. Gray dots represent the epicenters of the $M \geq 3$ aftershocks within the first 300 days and the yellow star indicates the main shock epicenter.

Mai (see http://www.seismo.ethz.ch/static/srcmod/). The ΔCFS values are calculated for a horizontal spatial grid with spacing of ~2 km, this is necessary to limit the calculation time. The same grid points are used for the calculation of the probability maps in the ShakeMap and all other models. For the calculation, we randomly selected $N = 100$ aftershock mechanisms and used $Z = 11$ depth layers between 3 and 13 km with a spacing of 1 km. Here we assumed that the mean strike and dip is in agreement with the main shock mechanism, while the rake was set to $-180°$ in agreement with the general right-lateral strike-slip regime in California. Furthermore, we assumed normal distributions for the strike, dip and rake values of the aftershock mechanisms according to *Hainzl et al.* [2010a], where the standard deviation was set to 20° in all cases. All information for Coulomb stress calculations are summarized in Table 2.

[25] Figures 1, 2, and 3 show the calculated probability maps and the observed aftershocks for the three test cases. It is clearly visible that the aftershock distributions are anisotropic and cluster around the fault traces of the main shocks. Modeling the aftershocks by an isotropic distribution, as done in the basic ETAS model, obviously leads to wrong forecasts. The anisotropic distributions related to the ShakeMap data and the GMM calculation are in general very similar, however, the GMM calculation leads to a smoother result. The map resulting from the ETAS spatial kernel evaluated relative to the nearest distance to the ruptured fault segment is also similar, however, it predicts a much stronger decay with distance than the forecasts based on the ground

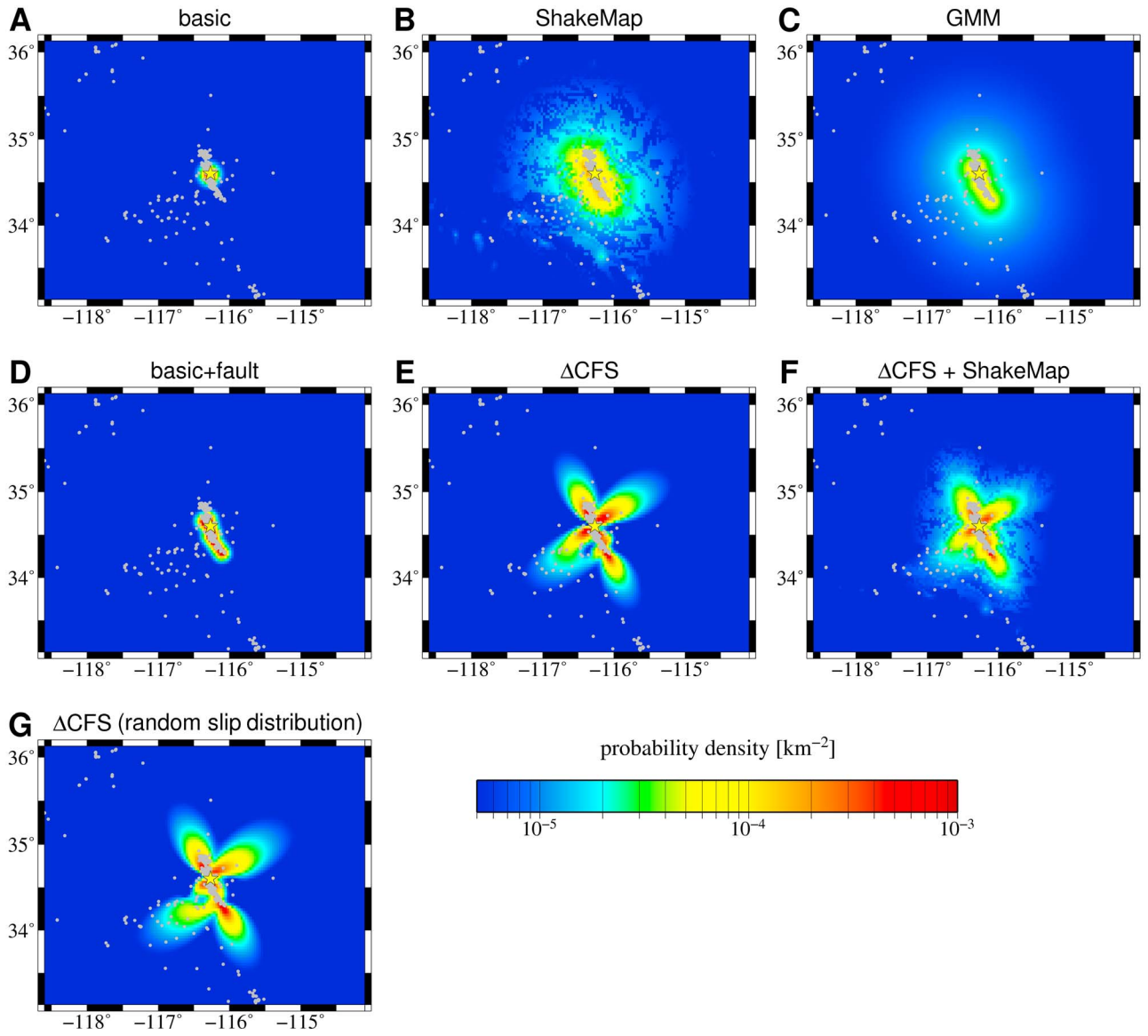

Figure 2. (a–g) Calculated probability maps for the Hector Mine earthquake (see Figure 1 for detailed description).

motion data (compare Figure 5). Completely different to the other distributions is the probability map based on static Coulomb stress changes, which is much more irregular. The map based on Coulomb stress changes using random slip distributions is very similar to the one using the published slip model.

[26] Although the visual comparison with the observed aftershocks can already give some hints about the forecasting ability of each model, a quantitative test has to be performed. This is in particular important because the probability maps describe only the spatial distribution of aftershocks directly triggered by the main shocks, while observed seismicity also includes background as well as secondary aftershock activity. This can also be seen in Figure 1. The cluster in the West (−116.8°W, 34.2°N) is mainly related to secondary aftershocks triggered by the M6.4 Big Bear event, the largest aftershock in this earthquake sequence. Note that in our ETAS model approach, this secondary cluster will be mainly attributed to the isotropic aftershock distribution of the Big Bear event and not to the Landers event. In sections 4 and 5, we describe the results for a comprehensive, comparative test of the different models.

4. Test

[27] In this section we discuss the extensions of the ETAS model using the different information related to the main shocks. The earthquake model is described by equation (3) where $f_m(\vec{x})$ is replaced by the different probability maps, displayed in Figure 1 for the example of the Landers main shock.

[28] To construct the tests more realistic, the optimization of the ETAS parameters is done only for events which occurred before the main shock. Consequently the resulting ETAS parameters used for all model applications are the

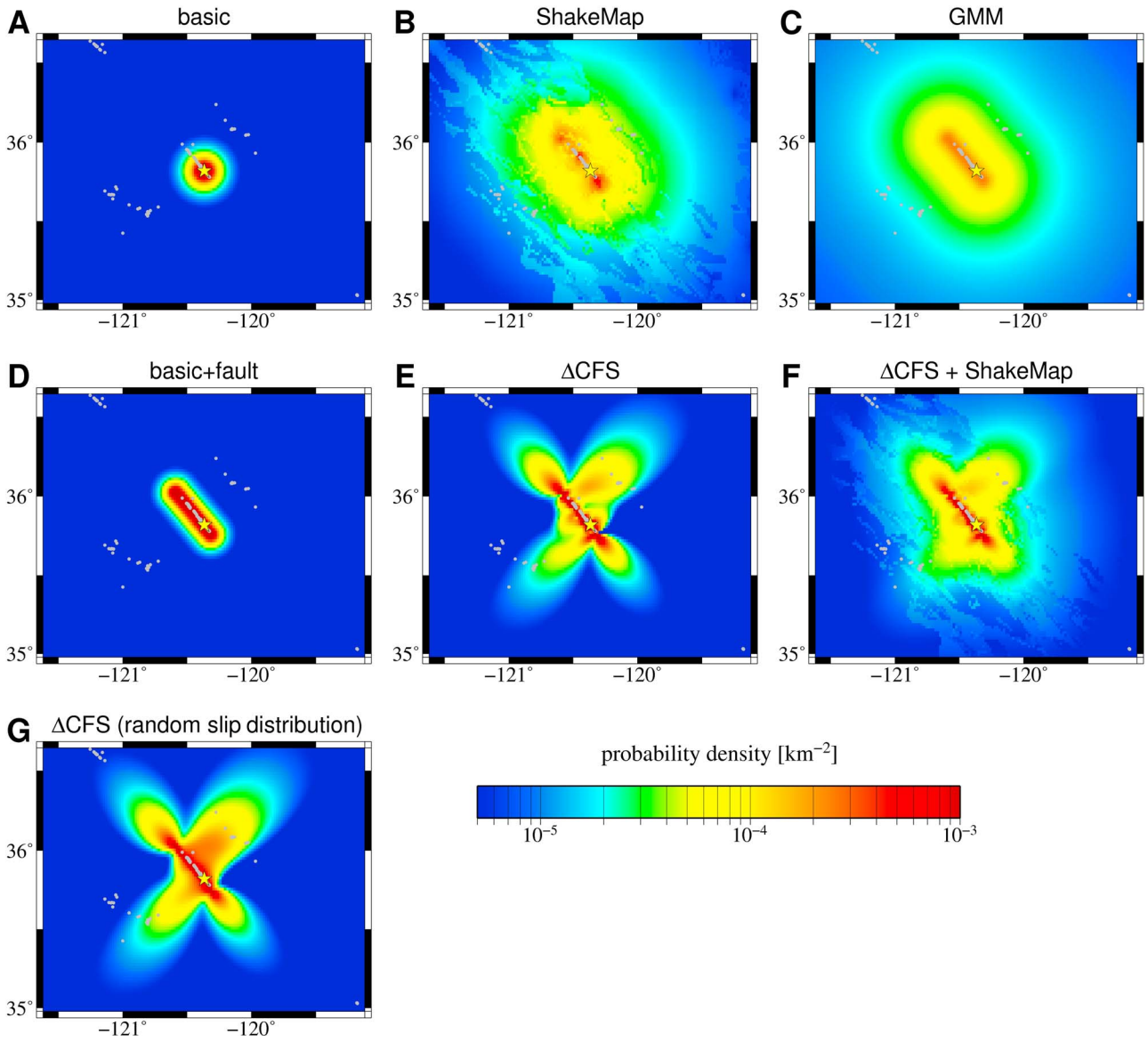

Figure 3. (a–g) Calculated probability maps for the Parkfield earthquake (see Figure 1 for detailed description).

same. We calculated the parameters $\theta = (\mu, K, c, \alpha, p, q, d)$ for the $M \geq 3$ events for a time period of 300 days before the main shock by maximizing the log likelihood function. The resulting parameter values and standard deviations for each of the three earthquake sequences are given together with the specifications of the space window in Table 3. The standard errors of estimated parameters were calculated from the Hessian matrix. Some α values are quite low, probably because of the low number of events in the optimization interval and the assumption of spatial isotropy of the earthquakes [*Hainzl et al.*, 2008]. To make sure this does not influence the results we tested the models also using fixed higher α values and inverting only the other parameters (see section 6). The ETAS parameters were then fixed for all models and used for the evaluation of the forecast ability of the $M \geq 3$ aftershocks which followed in the first 300 days after the main shock. For simplicity, times are given in the following always relative to the main shock occurrence time. Thus the optimization time interval is [−300, 0] days and the testing period is [0, 300] days. In each case, the investigated area was chosen according to the coverage of the ShakeMap and the grid size was limited to ∼2 km due to rapidly increasing calculation times of the Coulomb stress changes.

[29] We run two different tests. The first one is a forecast test (Test-A). In this case, earthquakes which occurred before the main shock are allowed to influence the aftershock probability, whereas observed aftershocks were not used to alter the forecasts. This test might reflect the case where forecasts have to be given directly after the main shock without any knowledge of aftershocks. The second test (Test-B) takes secondary aftershock triggering into account by using the information of the aftershock catalog. Thus, in this case, the consistency of the full model with the observations is quantified. The forecasted earthquake rate

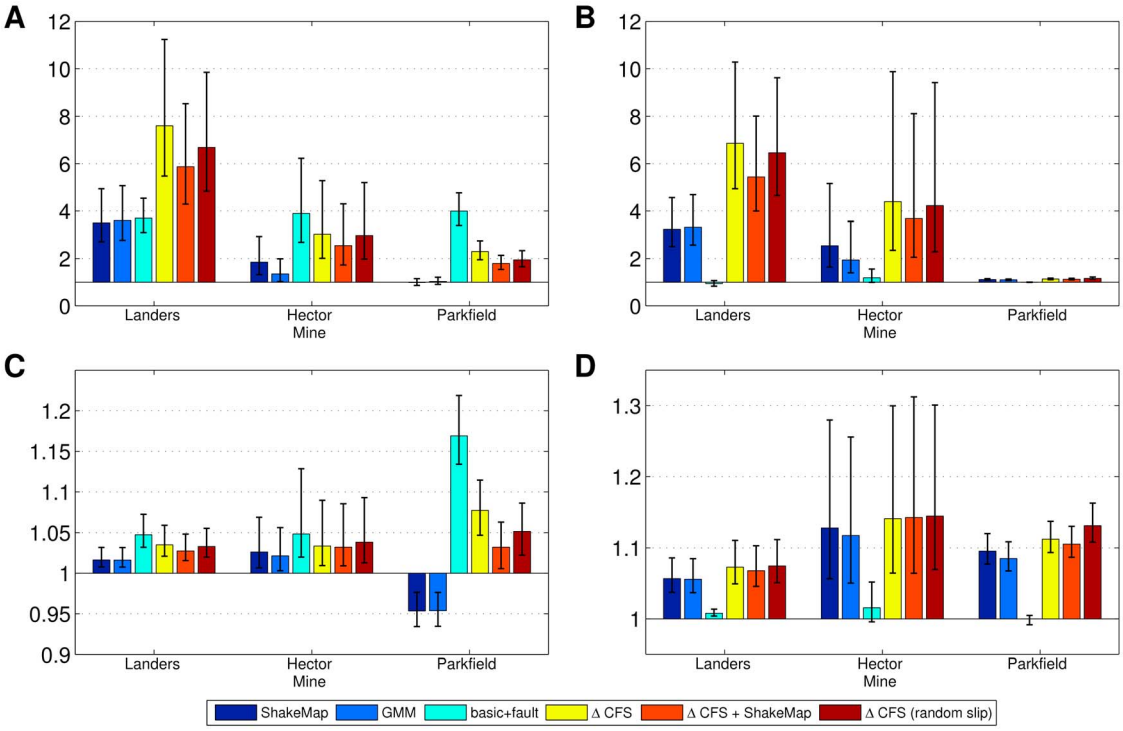

Figure 4. Probability gain for different models: Results of Test-A are shown for all events (a) in the target region and (b) for the off-fault ($r \geq 5$ km) only. (c, d) The corresponding results for the Test-B. Error bars define the 80% confidence interval for 1000 simulations with randomly chosen ETAS parameters (see description in section 6).

$\lambda(t, \vec{x})$ at a given time t in the test period, is given in Test-A by equation (3) where the right sum is limited to $t_k < 0$ while the sum is evaluated for $t_k \leq t$ in the second test.

[30] The test quantity in both cases is the log likelihood value of the models for the test period which is given by [*Ogata*, 1983]

$$\ln L = \sum_{i=1}^{N} \ln\lambda(t_i, x_i, y_i) - \int_S^T \iint_A \lambda(t, x, y) dx dy dt, \qquad (6)$$

where t_i are the occurrence times of the N events with $M \geq M_{\min}$ occurred in the test period $[S, T]$ and test region A. In the standard case, $M_{\min} = 3$, $S = 0$ and $T = 300$ days, while results for other values are discussed in section 6. For the comparison of the different hybrid models, we calculated the probability gain per event by $e^{\Delta \ln L/N}$. Here $\Delta \ln L$ is determined relative to the basic ETAS model, which facilitates the comparison of the different models and quantifies the improvement concerning the standard model. An information gain larger than one means, that the aftershock forecast is improved compared to the basic ETAS model, while values below one mean a worsening.

[31] Although most aftershocks usually occur close to the ruptured fault, future larger events might be expected to occur at more distant places, in particular, at neighboring fault segments or larger hidden faults. To take care of both cases, we test for two different target events. On the one hand, we calculated the log likelihood value for all aftershocks in the investigated area. In this case, the information gain is only related to the spatial forecast because all other model components are identical in the different models. On the other hand, the calculation was done only for aftershocks which occurred more than 5 km away from the rupture in order to compare the ability of forecasting off-fault activity. Note that this test includes not only spatial information but also total rate information because the models forecast different numbers of events in the tested off-fault region.

[32] To evaluate the robustness of our results, we repeated all tests for different cut-off magnitudes and different time windows. We also tested the use of fixed higher α values because the estimated values, especially for the Hector Mine sequence, are quite low. And we increased the optimization time interval for the parameter estimation to $[-3000, 0]$ days, because the estimation can be unstable for short intervals, and repeated the tests for the resulting parameter set.

5. Results

[33] We applied the test procedure to the three earthquake sequences described in section 3. The resulting probability gains for the two tests and the two different target events are displayed in Figure 4.

5.1. Test-A

[34] If we take all $M \geq 3$ aftershocks in the first 300 days into account (Figure 4a), ShakeMap and GMM data are able to improve the aftershock forecast for Landers and slightly for Hector Mine. For the Parkfield sequence, the more

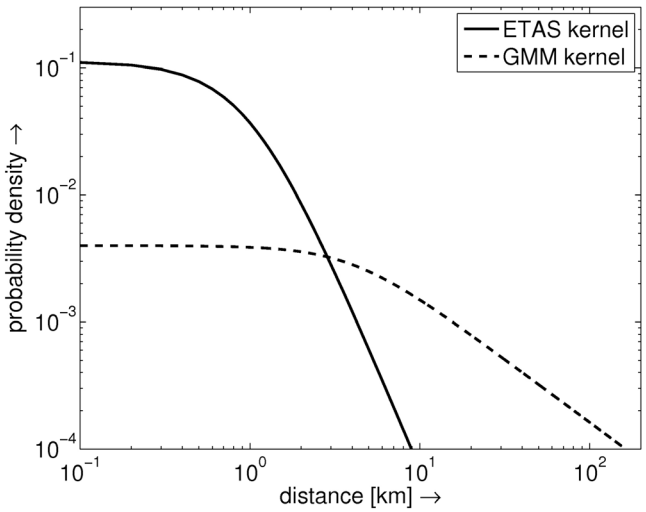

Figure 5. Comparison of the decay of the ETAS and the GMM kernel which are used for the $ETAS_{basic+fault}$ and the $ETAS_{GMM}$ model, respectively.

complex model performs nearly equal to the basic ETAS model. The reason seems to be that the decay of PGV values with distance to the fault is too weak to explain the large number of aftershocks very close to the fault. Compared to this, the ETAS decay function resulting from the fit of the precursory seismicity decays much faster with distance. Using this seismicity based function evaluated as a function of the nearest distance to the rupture (model $ETAS_{basic+fault}$) results in a larger improvement and the highest information gain for two of the earthquake sequences. We find that the use of Coulomb stress change maps improves the forecast ability best for the Landers sequence and second best for the other two sequences. The difference in using published or random slip distributions is mostly small. Anyway, the comparison with the ground-motion based forecasts shows that the static stress triggering models always outperform the dynamic stress triggering models. Also the combination of static and dynamic stress information could not improve the model performance any more.

[35] Figure 4b shows the probability gain obtained only using aftershocks more than 5 km away from the rupture area. It is found that the more distant aftershocks are best modeled using Coulomb stress change information. In contrast to the test for all aftershocks, the model $ETAS_{basic+fault}$ is the worst one and now even worse than the ShakeMap based model for all of the three earthquake sequences, indicating that off-fault aftershocks are decaying slower with distance than the more frequent aftershocks in the vicinity of the fault.

5.2. Test-B

[36] The corresponding results for this test are shown in Figures 4c and 4d. For this test, aftershock interactions are taken into account. This improves the $ETAS_{basic}$ model, so the probability gain in total is smaller than for the Test-A. ShakeMap and GMM data are not able to improve the model for all sequences, whereas the $ETAS_{basic+fault}$ model has the highest information gain. Coulomb stress change data can improve the model in all of the three cases. The same test using only aftershocks more than 5 km away from the rupture leads to similar results like the Test-A. All extensions are able to improve the model, but Coulomb stress change data improve the model most. Furthermore, it is interesting to note, that in some cases, the information gain using random slip distributions is even slightly better than using the published ones.

6. Discussion

[37] Testing the three earthquake sequences reveals the importance of knowing the main shock rupture geometry for aftershock forecasting. Based on this information only, the ETAS model can for two sequences best explain the near-fault aftershocks when the empirical seismicity based decay is evaluated as function of the nearest distance to the main shock rupture, i.e. the $ETAS_{basic+fault}$ model. The high information gain clarifies the need of a fast estimation of the fault geometry after a main shock, for example by fitting the locations of first aftershock recordings. This is already done in some aftershock models as in particular ETAS implementations [*Helmstetter et al.*, 2006; *Werner et al.*, 2011] and the STEP model [*Gerstenberger et al.*, 2005].

[38] Although the ground motions are also decaying with a similar decay law as used in the $ETAS_{basic+fault}$ model, the models based on ground-motion maps are found to describe the aftershock distributions worse. A possible explanation is the different gradient of the decay laws (Figure 5). The seismicity based probability decays much faster with increasing distance to the fault than the PGV values used in our models $ETAS_{ShakeMap}$ and $ETAS_{GMM}$. Thus most aftershocks are expected in the $ETAS_{basic+fault}$ model to occur close to the fault which seems to be obviously true.

[39] On the other hand, we have shown that for distances greater than 5 km, the $ETAS_{basic+fault}$ model performs worse than the models based on ground-motions or ΔCFS. In particular, Coulomb stress change maps are found to

Table 3. ETAS Parameters and Standard Deviations Calculated for the Three Earthquake Sequences Using 300 Days of $M \geq 3$ Pre-Main Shock Events[a]

	Latitude	Longitude	μ (days^{-1})	K	c (days)	α	p	q	d (km)
Landers	[33.2, 35.2]	[−117.9, −114.9]	0.08 ±0.018	0.053 ±0.006	0.002 ±0.0009	0.94 ±0.132	1.06 ±0.034	1.49 ±0.058	0.36 ±0.053
Hector Mine	[33.1, 36.1]	[−118.6, −114.1]	0.16 ±0.026	0.038 ±0.009	0.0002 ±0.0002	0.51 ±0.462	0.97 ±0.044	1.42 ±0.096	0.23 ±0.059
Parkfield	[35.0, 36.6]	[−121.6, −119.1]	0.05 ±0.015	0.06 ±0.006	0.01 ±0.0045	0.92 ±0.104	1.12 ±0.033	1.78 ±0.109	0.90 ±0.126

[a]The parameters are constant in the forecast interval for all models.

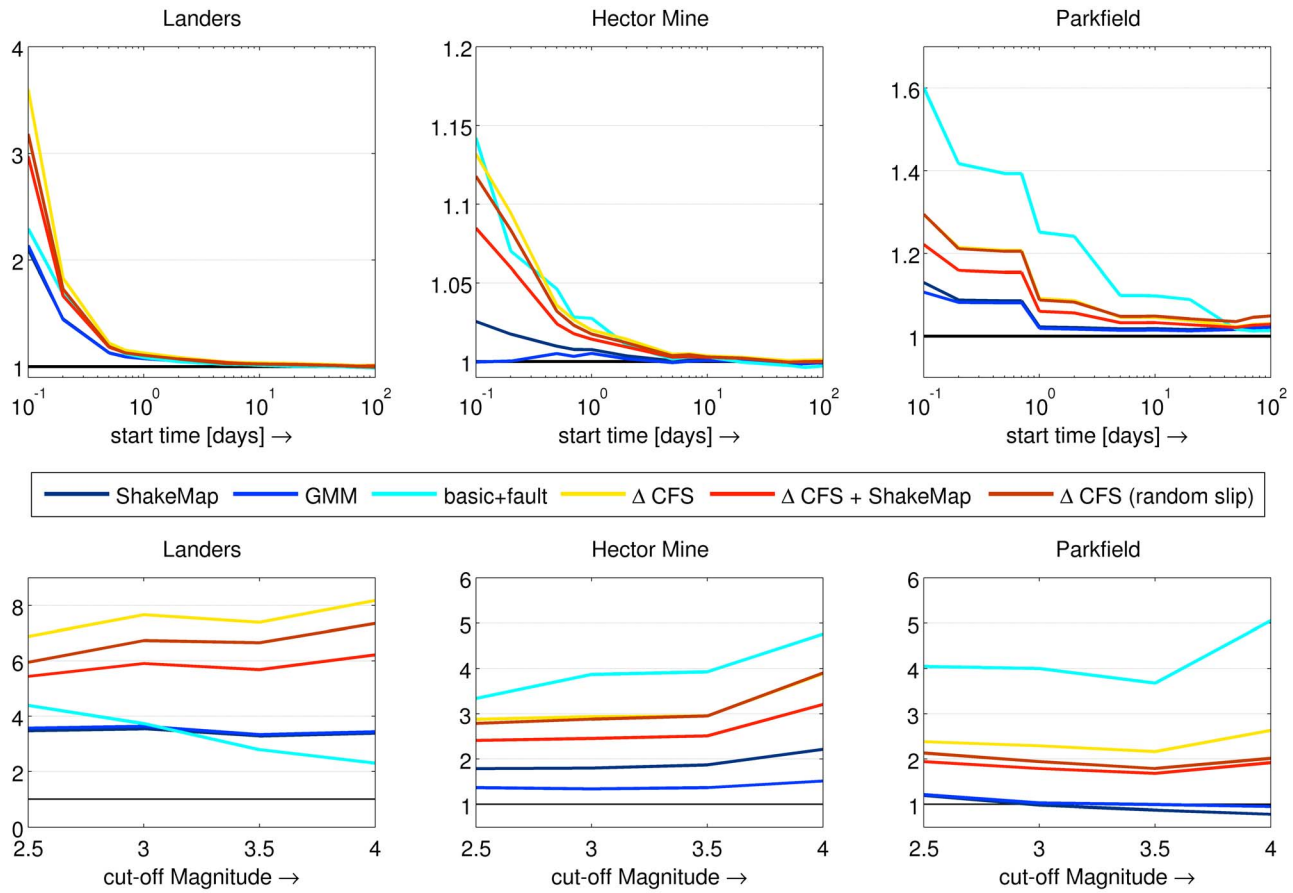

Figure 6. Results of the forecast test Test-A as a function of time and magnitude: (top) The probability gain per event as a function of the start time (the end of the analyzed time window is always 300 days), (bottom) the results as a function of the cut-off magnitude.

perform best for the more distant aftershocks, which is in agreement with *King et al.* [1994]. In this case, stress calculations are less affected by small-scale slip variability which is not resolvable by inversion of observational data and thus expected to be more accurate. This might explain why the static stress-triggering model works better for the more distant events than for the near-fault aftershocks. Using randomized slip models for Coulomb stress calculations in all cases leads to very similar results like using the published slip models. This is promising because in the first case no additional information besides rupture geometry and earthquake magnitude is needed.

[40] Tests show that our results are not affected by possible incomplete recordings of first aftershocks. For that we analyzed the information gain using different starting times of the test period, in particular S = 1 day and 10 days in equation (6), and thus excluding the first, probably incompletely recorded, events. We find the probability gains per event are slightly decreasing, however, the relative order of the models remains the same. Another test also focuses on the start time S of the forecast interval, but allowing first aftershocks, which occurred in the period [0, S] days, to influence the aftershock probability. This reflects the case that the forecast is updated after the occurrence of the first aftershocks. When changing the start time from $S = 0.1$ up to 100 days, the probability gain per event decreases significantly after the first day and slowly for the next weeks (Figure 6, top). This is likely related to the fact that the $\text{ETAS}_{\text{basic}}$ model adapts to the anisotropic aftershock distribution by using the first aftershocks. Having incorporated enough data, the forecast becomes very similar to the $\text{ETAS}_{\text{basic+fault}}$ model. Then the performance of all models is very similar, although the static stress triggering model is in all cases slightly better than the other models. This might be related to the increasing relative number of events occurring more distant to the fault for later times. Additional tests show, that the models are also quite robust concerning different target magnitudes (Figure 6, bottom). The probability gain for the extended models is increasing for larger cut-off magnitudes, the relative order of the models generally remains constant, just for the Landers sequence the $\text{ETAS}_{\text{basic+fault}}$ model performs worse for larger cut-off magnitudes.

[41] Unusual low α values might also influence the results. To test the influence of this parameter, we repeated all calculations for the case that only μ, K, c, p, q and d were estimated from the precursory seismicity while the α value was fixed to 1.84 (corresponding to a value of 0.8 for basis of 10). We find no significant differences of our results. We also tested the case that the optimization interval is increased to $[-3000, 0]$ days. In this case, some of the parameters changed slightly and the α value calculated for the Hector

Mine sequence becomes more realistic. Larger optimization intervals might stabilize the parameter inversion and are thus preferable. Concerning our test, however, we find that the different parameter estimations only slightly affected the values of the probability gain for the models without changing the relative ranking between the different models.

[42] Both tests indicate the robustness of our general findings against variations of particular ETAS parameters. To verify this results, we calculated the probability gain for 1000 model setups where the parameters were selected randomly from a normal distribution with mean and standard deviations displayed in Table 3. All parameters are allowed to vary at the same time. Because parameter correlations are not considered, the estimated standard errors may be overestimated. The error bars in Figure 4 show the interval between the 10% and 90% quantils of the resulting values. Although the uncertainty intervals are quite large, the ranking between the different models is much less affected. The changes of the probability gain are strongly correlated and the probability gain values vary almost simultaneously for all models if the ETAS parameters change. This is confirmed by linear correlation coefficients between 0.86 and 0.99 for Test-A. In 100% of the cases for Parkfield and 98% for Hector Mine, the relative order of the models does not change. For the Landers sequence, the order remains constant in 60% of the cases, while in 33% the only change is that the $ETAS_{ShakeMap}$ model performs slightly better than the $ETAS_{basic+fault}$ model.

[43] It is important to note that the static stress triggering model is found to outperform the ground-motion models in all cases. Furthermore, we find that the forecast ability of the ΔCFS model cannot be improved by combining it with dynamic stress maps. Also the use of different weights for the kernels could not improve the results much and no optimal weight could be found consistent for all aftershock sequences. This seems to indicate that static stress changes are the dominant physical mechanism for aftershocks in agreement with previous conclusions [*Hainzl et al.*, 2010b]. However, our result that the near-fault aftershocks are mostly best modeled by a simple decay function from the rupture area indicates that our incomplete knowledge of the rupture and the large uncertainties in the calculation of the stress changes limit the forecast ability on short spatial scales.

7. Conclusion

[44] We test the possibility of improving ETAS forecasts by incorporating additional main shock information which might be available within minutes to hours after the events. The ETAS model has been established as a kind of standard model for short-time earthquake clustering over the past years, however, the spatial model component is rather unsatisfactory because it predicts only isotropic aftershock clouds in clear contradiction to observations. This is due to the fact that the basic ETAS model only relies on point information, namely the time, epicenter and magnitude of the earthquakes. Here we tested the benefit of including additional information of the rupture geometry, recorded ShakeMaps and distributions.

[45] Our tests show, that using additional input information can improve the spatial aftershock forecasts in most cases. In describing the overall aftershock sequence best, we find that only the fault geometry is needed. Evaluating the empirical aftershock decay function as a function of the nearest distance to the extended source instead of the epicenter leads to a significant improvement of the forecasts. However, the more distant aftershocks are better fitted by the static Coulomb stress change maps. Because the largest aftershocks might be expected to occur on still unruptured neighboring known or unknown fault segments, the incorporation of ΔCFS calculations in the ETAS model seems to be promising. Finally, our tests show consistently that static stress triggering seem to better fit the observations than dynamic stress triggering.

[46] **Acknowledgments.** We thank M. J. Werner, one anonymous reviewer and the Associate Editor for the detailed and helpful comments. This work is part of the Potsdam Research Cluster for Georisk Analysis, Environmental Change and Sustainability (PROGRESS) project.

References

Campbell, K. W., and Y. Bozorgnia (2008), NGA ground motion model for the geometric mean horizontal component of PGA , PGV , PGD and 5% damped linear elastic response spectra for periods ranging from 0 . 01 to 10 s, *Earthquake Spectra*, *24*(1), 139–171, doi:10.1193/1.2857546.

Cocco, M., and J. R. Rice (2002), Pore pressure and poroelasticity effects in Coulomb stress analysis of earthquake interactions, *J. Geophys. Res.*, *107*(B2), 2030, doi:10.1029/2000JB000138.

Console, R., M. Murru, and A. M. Lombardi (2003), Refining earthquake clustering models, *J. Geophys. Res.*, *108*(B10), 2468, doi:10.1029/2002JB002130.

Console, R., M. Murru, and F. Catalli (2006), Physical and stochastic models of earthquake clustering, *Tectonophysics*, *417*(1–2), 141–153, doi:10.1016/j.tecto.2005.05.052.

Custódio, S., P. Liu, and R. J. Archuleta (2005), The 2004 M w 6.0 Parkfield, California, earthquake: Inversion of near-source ground motion using multiple data sets, *Geophys. Res. Lett.*, *32*, L23312, doi:10.1029/2005GL024417.

Gerstenberger, M. C., S. Wiemer, L. M. Jones, and P. A. Reasenberg (2005), Real-time forecasts of tomorrow's earthquakes in California, *Nature*, *435*, 328–331, doi:10.1038/nature03622.

Hainzl, S., A. Christophersen, and B. Enescu (2008), Impact of earthquake rupture extensions on parameter estimations of point-process models, *Bull. Seismol. Soc. Am.*, *98*(4), 2066–2072, doi:10.1785/0120070256.

Hainzl, S., B. Enescu, M. Cocco, J. Woessner, F. Catalli, R. Wang, and F. Roth (2009), Aftershock modeling based on uncertain stress calculations, *J. Geophys. Res.*, *114*, B05309, doi:10.1029/2008JB006011.

Hainzl, S., G. Zöller, and R. Wang (2010a), Impact of the receiver fault distribution on aftershock activity, *J. Geophys. Res.*, *115*, B05315, doi:10.1029/2008JB006224.

Hainzl, S., G. B. Brietzke, and G. Zöller (2010b), Quantitative earthquake forecasts resulting from static stress triggering, *J. Geophys. Res.*, *115*, B11311, doi:10.1029/2010JB007473.

Hardebeck, J. L., J. J. Nazareth, and E. Hauksson (1998), The static stress change triggering model: Constraints from two southern California aftershock sequences, *J. Geophys. Res.*, *103*, 103, 24,427–24,437.

Harris, R. A. (1998), Introduction to special section: Stress triggers, stress shadows, and implications for seismic hazard, *J. Geophys. Res.*, *103*(B10), 347–358.

Helmstetter, A., and D. Sornette (2002), Subcritical and supercritical regimes in epidemic models of earthquake aftershocks, *J. Geophys. Res.*, *107*(B10), 2237, doi:10.1029/2001JB001580.

Helmstetter, A., Y. Y. Kagan, and D. D. Jackson (2005), Importance of small earthquakes for stress transfers and earthquake triggering, *J. Geophys. Res.*, *110*, B05S08, doi:10.1029/2004JB003286.

Helmstetter, A., Y. Y. Kagan, and D. D. Jackson (2006), Comparison of short-term and time-independent earthquake forecast models for Southern California, *Bull. Seismol. Soc. Am.*, *96*(1), 90–106, doi:10.1785/0120050067.

Herrero, A., and P. Bernard (1994), A kinematic self-similar rupture process for earthquakes, *Bull. Seismol. Soc. Am.*, *84*(4), 1216–1228.

Ji, C. (2002), Source description of the 1999 Hector Mine, California, earthquake, part II: Complexity of slip history, *Bull. Seismol. Soc. Am.*, *92*(4), 1208–1226, doi:10.1785/0120000917.

King, G. C. P., R. S. Stein, and J. Lin (1994), Static stress changes and the triggering of earthquakes, *Bull. Seismol. Soc. Am.*, *84*(3), 935–953, doi:10.1016/0148-9062(95)94484-2.

Marsan, D. (2003), Triggering of seismicity at short timescales following Californian earthquakes, *J. Geophys. Res.*, *108*(B5), 2266, doi:10.1029/2002JB001946.

Marsan, D. (2006), Can coseismic stress variability suppress seismicity shadows? Insights from a rate-and-state friction model, *J. Geophys. Res.*, *111*, B06305, doi:10.1029/2005JB004060.

Marsan, D., and O. Lengliné (2008), Extending earthquakes' reach through cascading, *Science*, *319*(5866), 1076–1079, doi:10.1126/science.1148783.

Marsan, D., and O. Lengliné (2010), A new estimation of the decay of aftershock density with distance to the mainshock, *J. Geophys. Res.*, *115*, B09302, doi:10.1029/2009JB007119.

Nur, A., and J. R. Booker (1972), Aftershocks caused by pore fluid flow?, *Science*, *175*(4024), 885–887, doi:10.1126/science.175.4024.885.

Ogata, Y. (1983), Estimation of the parameters in the modified Omori formula for aftershock frequencies by the maximum likelihood procedure, *J. Phys. Earth*, *31*, 115–124.

Ogata, Y. (1988), Statistical models for earthquake occurrences and residual analysis for point processes, *J. Am. Stat. Assoc.*, *83*(401), 9–27.

Ogata, Y. (1998), Space-time point-process models for earthquake occurrences, *Ann. Inst. Stat. Math.*, *50*(2), 379–402.

Perfettini, H., and J.-P. Avouac (2007), Modeling afterslip and aftershocks following the 1992 Landers earthquake, *J. Geophys. Res.*, *112*, B07409, doi:10.1029/2006JB004399.

Shearer, P. M., E. Hauksson, and G. Lin (2005), Southern California hypocenter relocation with waveform cross-correlation, part 2: Results using source-specific station terms and cluster analysis, *Bull. Seismol. Soc. Am.*, *95*(3), 904–915, doi:10.1785/0120040168.

Steacy, S. (2004), Sensitivity of static stress calculations to the earthquake slip distribution, *J. Geophys. Res.*, *109*, B04303, doi:10.1029/2002JB002365.

Utsu, T., and A. Seki (1955), Relation between the area of aftershock region and the energy of the mainshock, *J. Seismol. Soc. Jpn.*, *7*, 233–240.

Utsu, T., Y. Ogata, and R. S. Matsu'ura (1995), The centenary of the Omori formula for a decay law of aftershock activity, *J. Phys. Earth*, *43*, 1–33.

van der Elst, N. J., and E. E. Brodsky (2010), Connecting near-field and far-field earthquake triggering to dynamic strain, *J. Geophys. Res.*, *115*, B07311, doi:10.1029/2009JB006681.

Wald, D. J., and T. H. Heaton (1994), Spatial and temporal distribution of slip for the 1992 Landers, California, earthquake, *Bull. Seismol. Soc. Am.*, *84*(3), 668–691.

Wald, D. J., K.-W. Lin, and V. Quitoriano (2008), Quantifying and qualifying USGS ShakeMap uncertainty, *U.S. Geol. Surv. Open File Rep.*, *2008-238*.

Wang, R., F. Lorenzo-Martín, and F. Roth (2006), PSGRN/PSCMP: A new code for calculating co- and post-seismic deformation, geoid and gravity changes based on the viscoelastic-gravitational dislocation theory, *Comput. Geosci.*, *32*(4), 527–541, doi:10.1016/j.cageo.2005.08.006.

Werner, M. J., A. Helmstetter, D. D. Jackson, and Y. Y. Kagan (2011), High-resolution long-term and short-term earthquake forecasts for California, *Bull. Seismol. Soc. Am.*, *101*(4), 1630–1648, doi:10.1785/0120090340.

Woessner, J., et al. (2011), A retrospective comparative forecast test on the 1992 Landers sequence, *J. Geophys. Res.*, *116*, B05305, doi:10.1029/2010JB007846.

C. Bach and S. Hainzl, Helmholtz Centre Potsdam, GFZ German Research Centre for Geosciences, Section 2.1, Telegrafenberg, D-14473 Potsdam, Germany. (bach@gfz-potsdam.de; hainzl@gfz-potsdam.de)